Journal of Non-Crystalline Solids 434 (2016) 1–12

Contents lists available at ScienceDirect

Journal of Non-Crystalline Solids

journal homepage: www.elsevier.com/locate/jnoncrysol

Bulk elastic properties, hardness and fatigue of calcium aluminosilicate glasses in the intermediate-silica range

A. Pönitzsch [a], M. Nofz [b], L. Wondraczek [c], J. Deubener [a,*]

[a] Institute of Non-Metallic Materials, Clausthal University of Technology, 38678 Clausthal-Zellerfeld, Germany
[b] Federal Institute of Materials Research and Testing (BAM), 12489, Berlin, Germany
[c] Otto-Schott-Institute of Materials Research, Friedrich Schiller University of Jena, 07743 Jena, Germany

ARTICLE INFO

Article history:
Received 2 October 2015
Received in revised form 6 December 2015
Accepted 17 December 2015
Available online 22 December 2015

Keywords:
Aluminosilicate glasses
Elastic constants
Indentation
Hardness
Crack initiation
Sub-critical crack growth

ABSTRACT

Bulk elastic properties, hardness and fatigue of calcium aluminosilicate (CAS) glasses in the technically relevant region of the ternary with intermediate-silica fraction were determined by combining results of Vickers indentation, ultrasonic echography and Archimedian buoyancy at room temperature. Of three studied compositional series, the first series was along the meta-aluminous join, while in the two other series the molar fraction of SiO_2 was kept constant. For the first series the elastic moduli and hardness show an almost linear increase with increasing SiO_2 fraction. In contrast, increasing the CaO/SiO_2 ratio at constant silica content results in a characteristic change when passing the meta-aluminous join. Elastic constants and hardness were lower at the percalcic than on the peraluminous side. Empirical models which relate bulk elastic moduli to internal energy, short-range inter-atomic forces and the packing density of their oxide constituents were found to be in agreement with the experimental data for meta-aluminous glasses, while deviations between the observed and predicted trends were evident for percalcic compositions. Empirical fatigue parameters such as the probability to initiate cracks after indentation reflect the bulk mechanical properties in the CAS system when conducted in inert atmosphere, but are otherwise clearly dominated by environmental effects.

1. Introduction

Glasses of the $CaO–Al_2O_3–SiO_2$ (CAS) system are considered for their optical properties and as high strength fibres in the low-silica range [1–3], for their use as glass-ceramics in the intermediate-silica range [4,5] and for their resistance to cracking in the high-silica range [6]. The short- to medium-range order of CAS glasses of all three silica ranges have been investigated using various spectroscopic techniques such as infrared reflectivity [7–9], Raman scattering [10,11], X-ray and neutron diffraction [12,13], X-ray absorption [10,14,15] and nuclear magnetic resonance spectroscopy [7,10,11,16,17]. These studies indicate that silicon and aluminium are usually tetrahedrally coordinated to oxygen in a network structure, while calcium is compensating the charge of the AlO_4-tetrahedra from an interstitial position. For percalcic glasses ($Al_2O_3/CaO < 1$) calcium is present in excess of aluminium and non-bridging oxygen (NBO) is formed. A preference of aluminium for fully polymerized structural units Q^4 is evident, which implies that the equilibrium reaction $2Q^3 \leftrightarrow Q^4 + Q^2$ is shifted to the right side with increasing Al/(Al + Si) ratio. In the Q^n-concept n (= 4, 3, 2, 1, and 0) is the number of bridging oxygen per tetrahedrally coordinated silicon and aluminium. For meta-aluminous glasses ($Al_2O_3/CaO = 1$) small fractions of NBO are present, due to 5-fold coordinated aluminium [18] and aluminium triclusters [13]. For peraluminous glasses ($Al_2O_3/CaO > 1$) the fraction of higher coordinated aluminium increases with increasing Al_2O_3/CaO ratio [10].

The short- and mid-range structure is expected to affect the bulk elastic constants since moduli are directly related to the inter-atomic forces and the packing density of their oxide constituents [19–22]. Interrelations between elastic constants and the chemical dependence of structure in the low-silica part of the CAS-system are established [2, 23,24], while, unexpectedly, a lack of systematic data is evident for the intermediate-silica range. Data on elasticity and hardness of percalcic and meta-aluminous glasses is available only sporadically [6,22,25]. This similarly holds for investigations of crack-generation in these glasses, which are presently limited to the high-silica range (where a change in the fictive temperature-independent mechanical properties close to 80 mol% silica was observed [6]).

To fill this gap, we present here a concise study of elastic constants, hardness, crack generation and propagation parameters of CAS glasses with intermediate-silica content of about 30–75 mol%. This has the purpose of identifying correlations between network topology and their elastic and micromechanical properties, which are to be expected in particular for compositions across the meta-aluminous join (from

* Corresponding author.
E-mail address: joachim.deubener@tu-clausthal.de (J. Deubener).

http://dx.doi.org/10.1016/j.jnoncrysol.2015.12.002

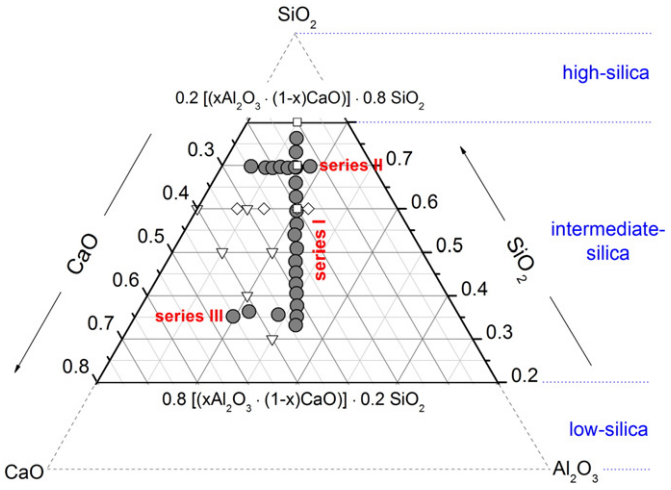

Fig. 1. $CaO–Al_2O_3–SiO_2$ (CAS) system as indicated by low-, intermediate- and high-silica ranges. Composition of glasses prepared for this study (solid circle) and those of Gross et al. [6] (open square), Inaba et al. [22] (open triangle) and Eagan and Swearekgen [25] (open diamond).

percalcic to peraluminous) [26]. The study, including three systematic series of totally 26 glasses (Fig. 1) provides a mechanistic understanding of the impact of constituting structural elements on bulk and near-surface mechanical properties of glasses of the basic calcium aluminosilicate system.

Table 1
Chemical analysis (LA-ICP), compositional ratios $S = Al/(Al + Si)$ and $R = 2Al/(Ca + 2Al)$, density ρ, molar volume V_M and atomic packing fraction *APF* of glasses of the series I–III. Numbers in parentheses give uncertainty of the last digit.

Composition (mol%)			S	R	ρ	V_M	*APF*
CaO	Al_2O_3	SiO_2			(g cm^{-3})	(cm^3 mol^{-1})	
Series I							
12.0	11.7	76.3	0.235	0.49	2.460(5)	26.19(5)	0.4874(9)
13.7	13.2	73.1	0.265	0.49	2.501(1)	25.98(1)	0.4925(2)
15.5	15.0	69.5	0.301	0.49	2.539(2)	25.87(2)	0.4967(3)
17.3	16.7	66.0	0.336	0.49	2.571(3)	25.79(3)	0.4998(6)
18.9	18.4	62.7	0.369	0.49	2.604(4)	25.72(4)	0.5032(7)
20.4	20.1	59.5	0.403	0.50	2.631(1)	25.70(1)	0.5065(2)
21.9	21.7	56.4	0.435	0.50	2.653(2)	25.72(2)	0.5071(3)
23.5	22.5	53.9	0.455	0.49	2.680(4)	25.54(4)	0.5099(7)
24.7	24.5	50.8	0.491	0.50	2.699(2)	25.67(1)	0.5110(4)
26.4	25.7	47.9	0.517	0.49	2.717(3)	25.67(3)	0.5117(5)
27.6	27.1	45.3	0.545	0.49	2.734(1)	25.71(1)	0.5127(2)
28.9	28.4	42.7	0.571	0.49	2.748(1)	25.75(2)	0.5131(2)
29.9	29.6	40.5	0.594	0.50	2.762(2)	25.79(2)	0.5140(3)
31.2	31.1	37.7	0.623	0.50	2.773(2)	25.89(2)	0.5137(4)
32.5	32.3	35.2	0.647	0.50	2.783(2)	25.96(2)	0.5135(4)
Series II							
24.3	5.9	69.7	0.145	0.19	2.602(3)	23.61(2)	0.5048(6)
21.6	8.9	69.4	0.204	0.29	2.580(4)	24.34(3)	0.5017(8)
20.2	10.4	69.4	0.231	0.34	2.567(2)	24.76(2)	0.4999(4)
18.5	11.8	69.6	0.253	0.39	2.556(1)	25.1(1)	0.4987(2)
17.2	13.4	69.4	0.278	0.44	2.545(3)	25.52(3)	0.4970(6)
15.6	14.8	69.6	0.298	0.48	2.538(2)	25.84(2)	0.4965(4)
12.5	17.7	69.8	0.336	0.59	2.536(1)	26.39(1)	0.4977(2)
Series III							
45.2	19.6	35.2	0.527	0.30	2.860(3)	23.26(2)	0.5162(5)
41.5	22.2	36.3	0.550	0.35	2.838(1)	23.84(1)	0.5178(2)
36.0	28.4	35.6	0.615	0.44	2.793(4)	25.24(3)	0.5132(7)
33.7	33.1	33.2	0.666	0.50	2.782(1)	26.08(1)	0.5115(2)

2. Experimental

2.1. Glass preparation and density

For determination of the micromechanical properties, CAS glasses of a previous study were used. Details on the type and quality of the raw materials used for the batch as well as on the melting and cooling conditions of the glasses are reported in Ref. [16]. Glass specimens were optically homogeneous with respect to bubbles, crystals and striae. The glasses were assigned to three compositional series. Fig. 1 shows the ternary $CaO–Al_2O_3–SiO_2$ system (in molar fractions) in which the studied glasses are indicated. Table 1 compiles the chemical composition and the ratios $S = Al/(Al + Si)$ and $R = 2Al/(2Al + Ca)$ of each glass. The ratio S is used to indicate the degree (from 0 to 1) of nominal substitution of aluminium for silicon in the network, while R shows the charge balanced ratio of network aluminium to interstitial calcium. Values of R other than 0.5 indicate nominal NBO formation. As an example one calculates for the glass of the molar composition 25% CaO, 25% Al_2O_3, 50% SiO_2 (equalling $CaAl_2Si_2O_8$, the anorthite-type glass) $S = 0.5$ (every second tetrahedron is nominally occupied by Al^{3+}) and $R = 0.5$ (nominally NBO-free).

The chemical composition of the glasses was determined using a laser ablation-inductively coupled plasma mass spectrometer system (Compex 110, Lambda Physik, Göttingen, Germany and Perkin Elmer Elan DRC II, Canada), transforming the measured intensities into concentrations by applying an external calibration standard (NBS610 NIST, USA) as well as an internal element standard (^{29}Si) and summing

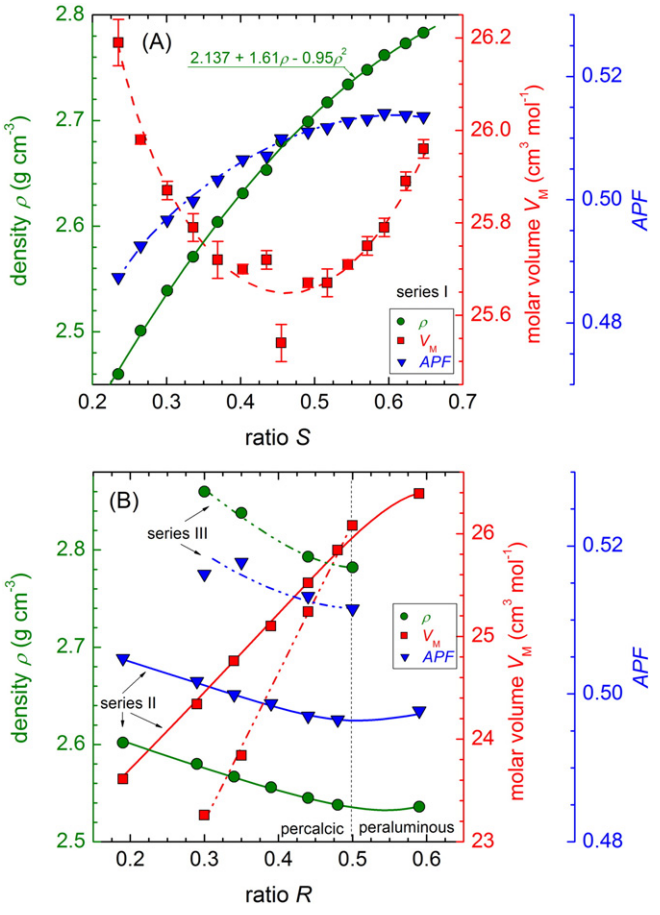

Fig. 2. Dependence of the density ρ, molar volume V_M and atomic packing fraction *APF* on the compositional ratios S (A) and R (B). Lines are intended as visual guides with the exception of $\rho(S)$ of series I, which is a quadratic polynomial fit through the data with the coefficient of determination $R^2 = 0.998$.

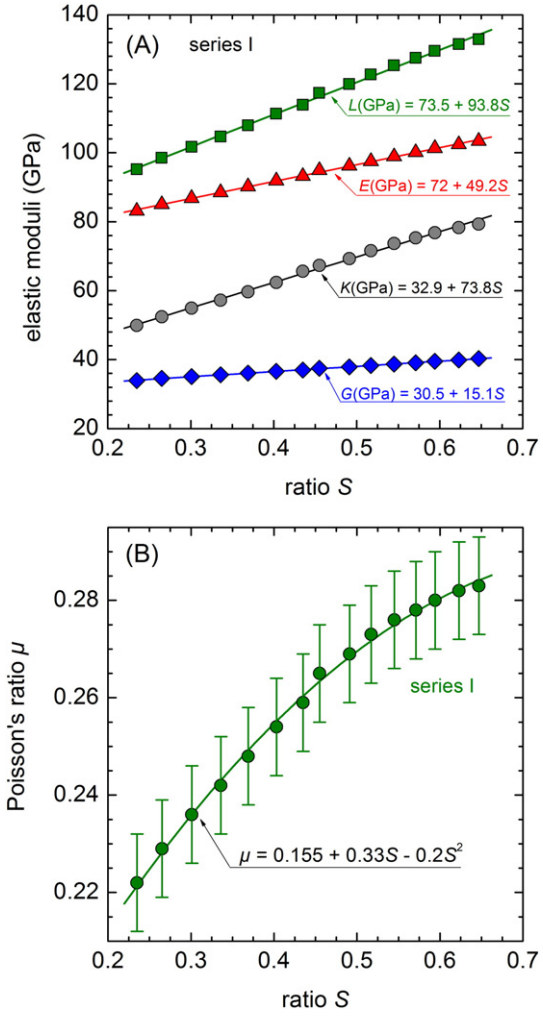

Fig. 3. Dependence of the elastic moduli L, E, K, and G (A) and Poisson's ratio μ (B) on the compositional ratio S (series I). The error bars of the elastic moduli do not exceed the size of the symbols. Lines are linear (L, E, K, G) and quadratic (μ) polynomial fits through the data with the coefficient of determination $R^2 = 0.998$, 0.999, 0.997, 0.999 and 0.995 for L, E, K, G and μ, respectively.

up all major elements to 100%. The error in the fractions of CaO, Al_2O_3 and SiO_2 was less than 0.1 mol%.

The density of the glasses ρ was determined at room temperature using the Archimedian buoyancy with ethanol as an immersion liquid. The error of this method (based on repetitive measurements) was ≤0.2%.

2.2. Elastic constants

Room temperature ultrasonic measurements were performed by a pulse-echo method with a USD 15S, Krautkramer Branson pulser–receiver instrument. Ultrasonic velocities v_l and v_s were determined from the specimen height h (7–10 mm) of two parallel faces (1 μm diamond, polished) and the delay time Δt_l and Δt_s between successive signals using 10 MHz and 4 MHz transducers for longitudinal (l) modes and for shear (s) modes, respectively [27,28]:

$$v_l = \frac{2h}{\Delta t_l} \text{ and } v_s = \frac{2h}{\Delta t_s}. \quad (1)$$

From the ultrasonic velocities elastic constants are calculated by [28,29]:

$$L = \rho \cdot v_l^2 \quad (2)$$

$$G = \rho \cdot v_s^2 \quad (3)$$

$$K = L - \frac{4}{3}G \quad (4)$$

$$E = \frac{9KG}{3K + G} \quad (5)$$

$$\mu = \frac{E}{2G} - 1 \quad (6)$$

with ρ = density, μ = Poisson's ratio and L, G, K and E = longitudinal, shear, compression and Young's moduli, respectively. The errors of this method (based on repetitive measurements) were ≤0.15% and ≤0.25% for the longitudinal and shear ultrasonic velocities, respectively.

2.3. Vickers hardness and crack initiation probability

Hardness was determined by Vickers indentation (Shimadzu HMV-2000, Kyoto, Japan) under ambient conditions (RH ≈ 50%, T = 20 °C) using a load of 9.81 N for which indentation size effects can be neglected [30–32]. For each glass the average diagonal length 2a of 20 imprints was measured immediately following unloading using a 3-D laser

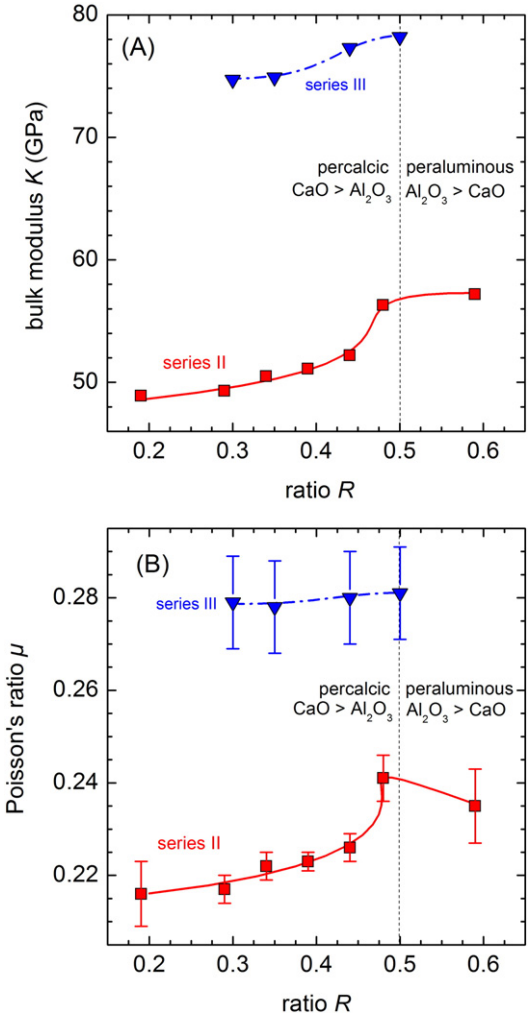

Fig. 4. Dependence of the bulk modulus K (A) and Poisson's ratio μ (B) on the compositional ratio S of glasses of series II and III. The error bars of the K data do not exceed the size of the symbols. Lines are intended as visual guides.

scanning microscope (VK-9700K, Keyence). Vickers hardness is given by [33,34]

$$H_V = \frac{P}{2.157 \times 10^{-3} a^2} \tag{7}$$

where H_V is the Vickers hardness (GPa), P is the applied load (N), and a is the average half diagonal of the indent (μm).

To cover a broad load range (0.2–20 N) crack initiation was studied using two different Vickers indenters (Shimadzu HMV-2000, Kyoto, Japan and UNAT-M ASMEC, Radeberg, Germany). The number of radial-median corner cracks was counted (35 indents per load for series I–II, 20 indents per load for series III) 24 h after indentation to allow for sub-critical crack growth. Wada et al. [35] first showed that the number of radial cracks increases with increasing indentation load in a sigmoidal-like course. The probability of crack initiation follows Weibull's statistics [36,37]:

$$F(P) = 1 - \exp\left[-\left(\frac{P - P_0}{\beta}\right)^m\right] \tag{8}$$

where P_0 is the critical load to generate radial corner cracks, β is the scale parameter and m is the Weibull modulus. According to Wada et al. [35] the crack resistance (CR) is defined as the load required to generate in average two out of four radial cracks, i.e. $F(P) = 0.5$.

To determine the effect of humidity [38] crack initiation was studied under ambient condition (RH ≈ 50%) and under dry nitrogen gas (glove box) at room temperature (20 °C). For the latter the glove box was equipped with the Vickers indenter, laser scanning microscope and an alumina type capacitive moisture sensor. The glove box was operated under relative humidity 10^{-4}–10^{-6}% RH, which corresponds to a moisture dew point in the range from −80 to −110 °C. 10 indents per load were performed for each glass series.

2.4. Sub-critical crack growth

Sub-critical crack growth was determined from selected radial cracks under ambient conditions (RH ≈ 50%, T = 20 °C). Immediately after indenting (P = 9.81 N for series 1–2 and P = 4.905 N for series 3) the glass was transferred within one minute to the 3-D laser scanning microscope (VK-9700K, Keyence) and the crack length c was measured over time for up to 47 min. The crack growth rate V was determined using the equations [38–40]:

$$c = A_1 t^n \tag{9}$$

and its first time-derivative

$$\frac{dc}{dt} = V = nA_1 t^{n-1} \tag{10}$$

where n is the growth exponent and A_1 is a constant. For each crack length of the corner cracks a stress intensity factor K_{IFT} was calculated [33,41]

$$K_{IFT} = 0.129\left(\frac{c}{a}\right)^{-3/2}\left(\frac{H_V\sqrt{a}}{\phi}\right)\left(\frac{H_V}{E\phi}\right)^{-2/5} \tag{11}$$

with the geometrical factor $\varphi = 3$. Eq. (11) requires a crack length-to-indent half diagonal ratio $c/a > 2.5$, which was the case for all corner cracks in the observation period (56–2820 s). We want to point out that the indentation fracture toughness K_{IFT} calculated from Eq. (11) is not comparable to fracture toughness obtained by standard methods. This has been clearly show for polycrystalline ceramics by Quinn and Bradt [42], where fracture toughness determined using length and applied load in Vickers indentation cannot reproduce the fracture toughness of standardized tests correctly. In those materials K_{IFT}

Table 2
Ultrasonic velocities v_l and v_s (Eq. (1)) and elastic constants L, G, K, E and μ (Eqs. (2)–(6)) of glasses of the series I–III. Numbers in parentheses give uncertainty of the last digit.

Glass		v_l	v_s	L	G	K	E	μ
S	R	(km s^{-1})	(km s^{-1})	(GPa)	(GPa)	(GPa)	(GPa)	
Series I								
0.235	0.49	6.222(9)	3.716(6)	95.2(3)	33.97(9)	49.9(4)	83.1(9)	0.22(1)
0.265	0.49	6.276(9)	3.718(5)	98.5(3)	34.57(9)	52.4(4)	85.0(9)	0.22(1)
0.301	0.49	6.330(9)	3.719(3)	101.7(3)	35.12(5)	54.9(4)	86.8(9)	0.23(1)
0.336	0.49	6.381(9)	3.722(1)	104.7(3)	35.63(1)	57.2(3)	88.5(9)	0.24(1)
0.369	0.49	6.439(4)	3.725(5)	107.9(1)	36.13(9)	59.7(3)	90.2(4)	0.25(1)
0.403	0.50	6.498(9)	3.729(4)	111.3(1)	36.65(1)	62.4(3)	91.9(7)	0.25(1)
0.435	0.50	6.552(9)	3.734(3)	113.9(2)	37.02(3)	65.6(3)	93.2(8)	0.26(1)
0.455	0.49	6.615(8)	3.741(9)	117.3(3)	37.52(9)	67.3(5)	94.9(8)	0.26(1)
0.491	0.50	6.665(9)	3.748(9)	119.9(3)	37.92(9)	69.3(5)	96.2(9)	0.27(1)
0.517	0.49	6.720(5)	3.755(5)	122.7(1)	38.32(9)	71.6(3)	97.5(5)	0.27(1)
0.545	0.49	6.770(9)	3.764(3)	125.3(3)	38.74(6)	73.7(4)	98.9(8)	0.28(1)
0.571	0.49	6.812(9)	3.774(3)	127.5(3)	39.14(5)	75.3(4)	100.1(8)	0.28(1)
0.594	0.50	6.849(8)	3.784(3)	129.5(3)	39.55(6)	76.8(4)	101.3(7)	0.28(1)
0.623	0.50	6.887(5)	3.795(3)	131.5(2)	39.95(5)	78.3(3)	102.4(5)	0.28(1)
0.647	0.50	6.912(9)	3.805(5)	132.9(3)	40.30(9)	79.3(5)	103.4(9)	0.28(1)
Series II								
0.145	0.19	6.030(9)	3.630(5)	94.7(3)	34.2(1)	48.9(2)	83.4(7)	0.216(7)
0.204	0.29	6.071(9)	3.648(9)	95.1(3)	34.3(2)	49.3(1)	83.6(7)	0.217(3)
0.231	0.34	6.130(9)	3.664(9)	96.5(3)	34.4(2)	50.5(1)	84.3(7)	0.222(3)
0.253	0.39	6.170(8)	3.683(9)	97.3(3)	34.6(2)	51.1(1)	84.8(6)	0.223(2)
0.278	0.44	6.227(9)	3.702(9)	98.7(3)	34.8(2)	52.2(1)	85.6(7)	0.226(3)
0.298	0.48	6.374(7)	3.720(9)	103.2(2)	35.1(2)	56.3(1)	87.2(5)	0.241(5)
0.336	0.59	6.474(9)	3.810(3)	106.3(3)	36.2(1)	57.2(2)	90.9(8)	0.235(8)
Series III								
0.527	0.30	6.643(9)	3.675(4)	126.2(3)	38.6(1)	74.7(5)	98.9(9)	0.28(1)
0.550	0.35	6.685(9)	3.704(4)	126.9(3)	38.9(1)	74.9(5)	99.6(9)	0.28(1)
0.615	0.44	6.833(9)	3.775(8)	130.4(3)	39.8(2)	77.3(6)	101.9(9)	0.28(1)
0.666	0.50	6.879(9)	3.795(4)	131.7(3)	40.0(1)	78.2(5)	102.7(9)	0.28(1)

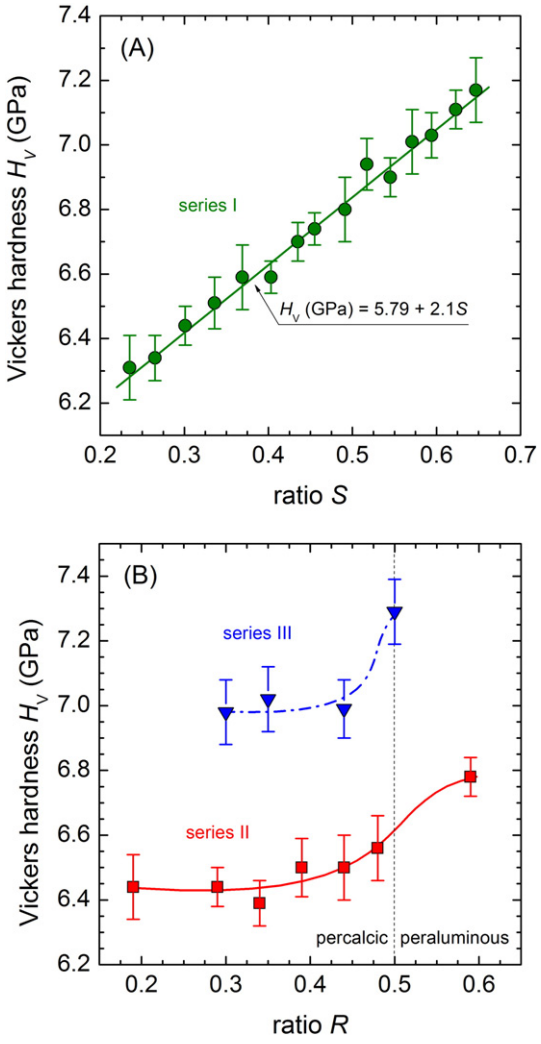

Fig. 5. Dependence of the Vickers hardness (9.81 N) on the compositional ratios *S* (A) and *R* (B). Line in the H_V vs. *S* diagram is linear fit through the data with the coefficient of determination $R^2 = 0.998$. Lines in the H_V vs. *R* diagram are intended as visual guides.

corresponds to a single point on the R-curve, which is different to that of the standard tests and should therefore only be used for internal comparison. For homogeneous glasses, however, extrinsic and intrinsic microstructural toughening behind and ahead of the crack tip, respectively, are absent [43]. Thus, Vullo and Davis [44] could show that the results obtained for oxide glasses from different chemical systems using the indentation method are sufficiently well correlated with fracture toughness values measured using standard techniques (Chevron notch).

The crack growth rate *V* was plotted as a function of calculated stress intensity factor K_{IFT} and fitted according to the empirical Paris' law [45]

$$V = A_2 K_{IFT}^{N} \tag{12}$$

where A_2 is a constant and *N* is the fatigue parameter, which describes the glasses' resistance to fatigue, or more precisely, to the corrosive power of the surrounding atmosphere.

2.5. Brittleness

Crack initiation phenomena in glassy systems can be linked to the empirical brittleness of glass as introduced by Lawn and Marshall [33]. They defined an index of brittleness as the ratio of hardness-to-toughness as

$$B = \frac{H_V}{K_{IFT}}. \tag{13}$$

3. Calculation

From density and chemical composition the molar volume V_M of the glass was calculated as

$$V_M = \frac{1}{\rho}\sum_i x_i M_i \tag{14}$$

with x_i and M_i being respectively the mole fraction and molar mass of the oxide *i*. The molar volume was utilized to determine the atomic packing fraction *APF*, which is a measure of the compactness of the glasses and defined as the ratio between the summed volume of the individual atoms and the corresponding volume of the glassy material. *APF* is calculated using the expression

$$APF = \frac{1}{V_M}\sum_i x_i V_i \tag{15}$$

where $V_i = 4\pi N_a(jr_A^3 + kr_O^3)/3$ is the ionic volume the *i*th oxide constituent (N_A = Avogadro number and r_i is the ionic radius using 135 pm (O^{II}), 100 pm (Ca^{VI}), 39 pm (Al^{IV}) and 26 pm (Si^{IV}) [46]) with A_jO_k

Table 3
Vickers hardness H_v, *c*/*a*-ratio ($P = 9.81$ N, 24 h after indentation), growth exponent *n*, constant A_1, fatigue resistance *N*, indentation fracture toughness K_{IFT} ($P = 9.81$ N, 24 h after indentation) and brittleness index *B* of glasses of the series I–III in air (≈50% RH, 20 °C). Numbers in parentheses give uncertainty of the last digit.

Glass		H_v	*c*/*a*	log A_1	*n*	*N*	K_{IFT}	*B*
S	*R*	(GPa)					(MPa m$^{1/2}$)	(μm$^{-0.5}$)
Series I								
0.235	0.49	6.3(1)	2.7(1)	1.82(2)	0.016(2)	51(5)	1.38(6)	4.5(3)
0.265	0.49	6.34(7)	2.7(1)				1.40(7)	4.5(2)
0.301	0.49	6.44(6)	2.8(1)				1.34(6)	4.8(2)
0.336	0.49	6.51(8)	2.8(1)				1.36(6)	4.8(3)
0.369	0.49	6.6(1)	2.9(1)	1.85(2)	0.012(1)	54(7)	1.30(5)	5.1(3)
0.403	0.50	6.59(5)	2.9(1)				1.32(6)	5.0(2)
0.435	0.50	6.70(6)	3.0(1)				1.26(5)	5.3(3)
0.455	0.49	6.74(5)	3.0(1)				1.27(5)	5.3(3)
0.491	0.50	6.8(1)	3.0(1)	1.88(1)	0.009(1)	65(6)	1.22(5)	5.3(3)
0.517	0.49	6.94(8)	3.0(1)				1.28(5)	5.3(3)
0.545	0.49	6.90(6)	3.1(1)				1.30(5)	5.6(3)
0.571	0.49	7.0(1)	3.1(1)	1.89(3)	0.008(1)	78(7)	1.24(5)	5.6(3)
0.594	0.50	7.03(7)	3.1(1)				1.26(5)	5.6(3)
0.623	0.50	7.11(6)	3.2(1)				1.21(5)	5.9(3)
0.647	0.50	7.2(1)	3.2(1)	1.89(1)	0.006(2)	85(7)	1.22(4)	5.9(3)
Series II								
0.145	0.19	6.4(1)	3.0(1)	1.84(3)	0.018(2)	31(5)	1.18(5)	5.4(3)
0.204	0.29	6.44(6)	2.8(1)	1.82(2)	0.017(2)	35(7)	1.32(6)	4.9(3)
0.231	0.34	6.39(7)	2.9(1)				1.25(5)	5.1(3)
0.253	0.39	6.50(9)	2.7(1)	1.81(1)	0.012(2)	46(5)	1.41(6)	4.6(3)
0.278	0.44	6.5(1)	2.8(1)				1.33(6)	4.9(3)
0.298	0.48	6.6(1)	2.6(1)	1.82(2)	0.012(1)	52(8)	1.52(7)	4.3(3)
0.336	0.59	6.78(6)	2.6(1)	1.79(1)	0.011(2)	55(7)	1.55(8)	4.4(3)
Series III								
0.527	0.30	6.9(1)	3.4(1)	1.71(2)	0.014(3)	41(8)	1.08(4)	6.3(3)
0.550	0.35	7.0(1)	3.4(1)	1.72(2)	0.011(1)	53(5)	1.09(4)	6.4(3)
0.615	0.44	6.99(9)	3.3(1)	1.71(2)	0.011(3)	64(5)	1.15(4)	6.0(3)
0.666	0.50	7.3(1)	3.1(1)	1.69(2)	0.009(2)	78(9)	1.29(5)	5.6(3)

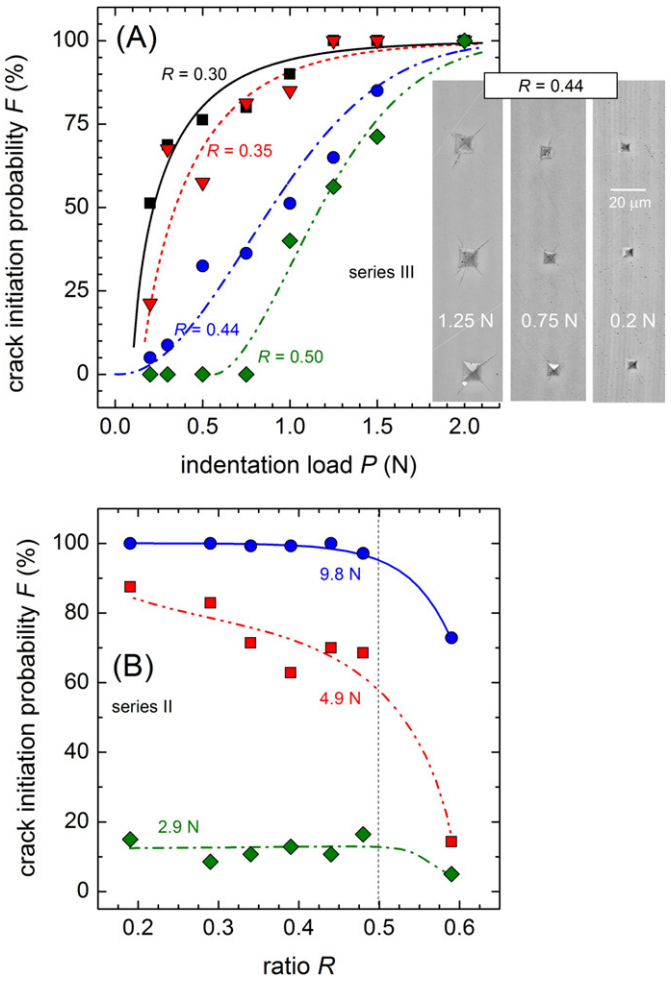

Fig. 6. Dependence of the crack initiation probability F as a function of applied load P for series III (A, left side). Lines in part A are fits of Weibull function Eq. (8) through the data. Cracking pattern around three indents after indentation under $P = 0.2$, 0.7 and 1.2 N for glass $R = 0.44$ (insert of A, right side). Crack initiation probability F vs. compositional ratio S for series II after indentation under $P = 9.8$, 4.9 and 3 N (B). Lines in part B are intended as visual guides.

chemical formula. For the calculation of Young's modulus the general equation [22]:

$$E = 2mV_P U \tag{16}$$

was used with the apparent Madelung constant m, the packing fraction V_P and the dissociation energy per unit volume U ($U = \Sigma x_i U_i$ with $U_i =$ dissociation energy of the oxide component in kcal cm^{-3}: CaO = 15.5, Al_2O_3 = 32, and SiO_2 = 15.4 [19]) In the Makishima–Mackenzie (MM) model [19] the packing fraction V_P is.

$$V_P = APF = \rho \frac{\sum_i x_i V_i}{\sum_i x_i M_i}, \tag{17}$$

which was calculated from Eqs. (14)–(15) whereas the Rocherulle–Ecolivet–Poulain–Verdier–Laurent (REPVL) model [21] uses the packing fraction:

$$V_P = \sum_i APF_i = \sum_i x_i \rho_i \frac{\sum_i x_i V_i}{\sum_i x_i M_i} \tag{18}$$

in which the density of the glass ρ is substituted by the weighted sum of the densities of the oxide components ρ_i ($APF_{CaO} = 0.8333$, $APF_{Al2O3} = 0.8333$ and $APF_{SiO2} = 0.6174$ [21]). In contrast to the above two models where m is unity, the Inaba–Todaka–Otha–Morinaga (ITOM) model [22] gives $m = 1.1$ for aluminosilicate glasses containing bivalent modifier ions such as Ca^{2+}. V_P in the ITOM model is calculated from Eq. (17) [22].

4. Results

4.1. Density, molar volume and atomic packing fraction

Experimental results obtained on CAS glasses of series I–III are summarized in Table 1. For series I, the density increases with increasing S from 2.46 to 2.783 g cm^{-3} and can be described best with a quadratic polynomial $\rho = 2.137 + 1.61S - S^2$, while the molar volume exhibits a parabolic curve shape with a minimum of ≈25.6 cm^3 mol^{-1} at around $S = 0.5$ (Fig. 2A). The compactness of the glass network, i.e., the atomic packing factor APF, shows the same trend as the density, increasing from 48.7 to 51.4%. For the series II and III, the change in composition from percalcic to peraluminous results in a decrease in density and APF, but an increase in molar volume. The curves of Fig. 2B appear to be slightly bended (series II) with a somewhat smaller slope around the meta-aluminous join ($S = 0.5$). The variation of V_M with S of series II and III was found to be larger (from 23.3 to 26.4 cm^3 mol^{-1}) than for series I ($\Delta V_M \approx 0.6$ cm^3 mol^{-1}). The data are in agreement with

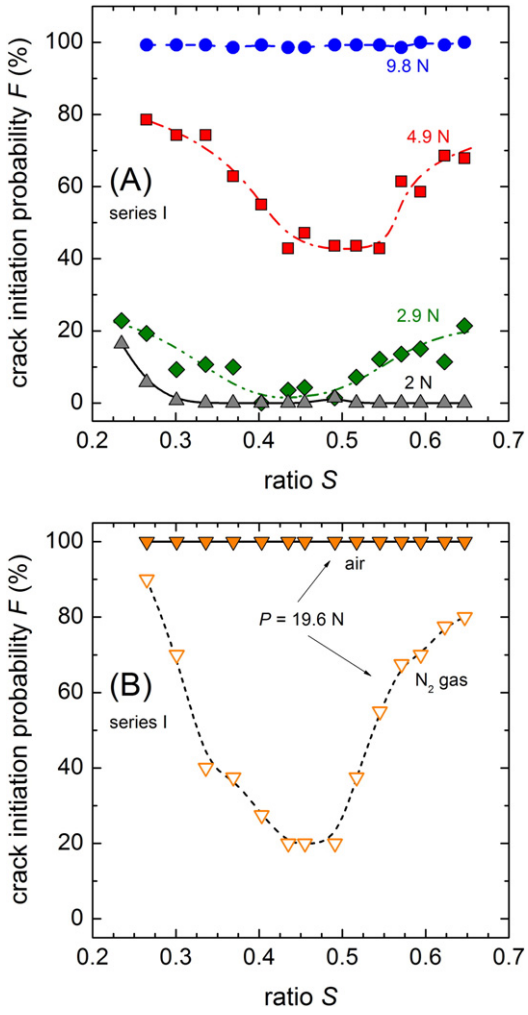

Fig. 7. Dependence of the crack initiation probability F on the compositional ratio S (series I) after indentation under $P = 9.8$, 4.9, 3 and 2 N in humid air (A) and after indentation under $P = 19.6$ N in humid air and in dry N_2 gas (B). Lines are intended as visual guides.

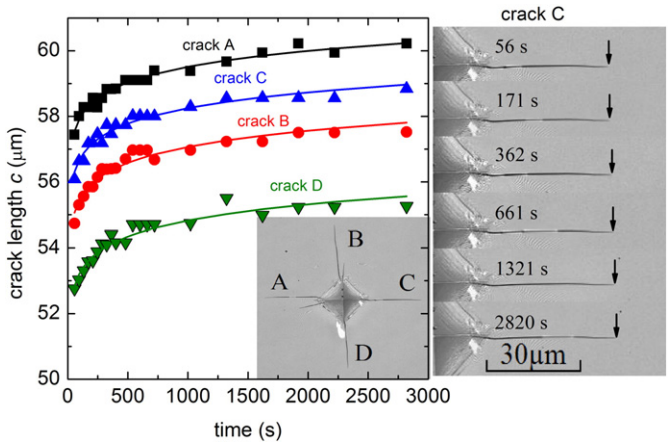

Fig. 8. Crack length c as a function of time of four corner cracks. Lower inset is an optical image, which shows the position of the four cracks (A–D) around the indent. Right inset shows optical images of the crack C in the time period 56–2820 s. The crack-tip is indicated by black arrows. In case of initial crack-branching (A and B corners) only sub-critical crack growth of the longest branch was measured. (Series III glass with $R = 0.35$, indentation load = 4.9 N, humid air of ≈50% RH and 20 °C).

measurements on density and calculations of molar volume and compactness of CAS glasses in the percalcic and peraluminous range by Takahashi et al. [9] and on the meta-aluminous join by Seifert et al. [47].

4.2. Elastic constants

Fig. 3A shows the elastic moduli and Poisson's ratio along the meta-aluminous join (series I). The former increase continuously with increasing substitution of aluminium for silicon in the network. A linear dependence within the range $0.23 < S < 0.65$ is evident. Linear fits with $L = 73.5 + 93.8S$, $E = 72 + 49.2S$, $K = 32.9 + 73.8S$ and $G = 30.5 + 15.1S$ (elastic constants in GPa) are found to describe best these compositional trends. Regarding Poisson's ratio, the curve flattens-out above $S = 0.5$. Here, the dependence of μ on S can be described best with a quadratic polynomial $\mu = 0.155 + 0.33S - 0.2S^2$ (Fig. 3B). For glass compositions across the meta-aluminous join a step-like course of K and μ on R is evident (Fig. 4A and B). For $SiO_2 \approx 70$ mol% (series II) the step at $R \approx 0.5$ is well pronounced while for glasses with less silica (≈35 mol% SiO_2, series III) the step appears to flatten-out. The other elastic constants (E, L and G) follow the same compositional trend (not shown). Ultrasonic velocities and elastic constants of series I–III glasses are compiled in Table 2.

4.3. Vickers hardness

The courses of Vickers hardness with increasing S and R are shown in Fig. 5. H_V is found to evolve in line with the elastic moduli as hardness

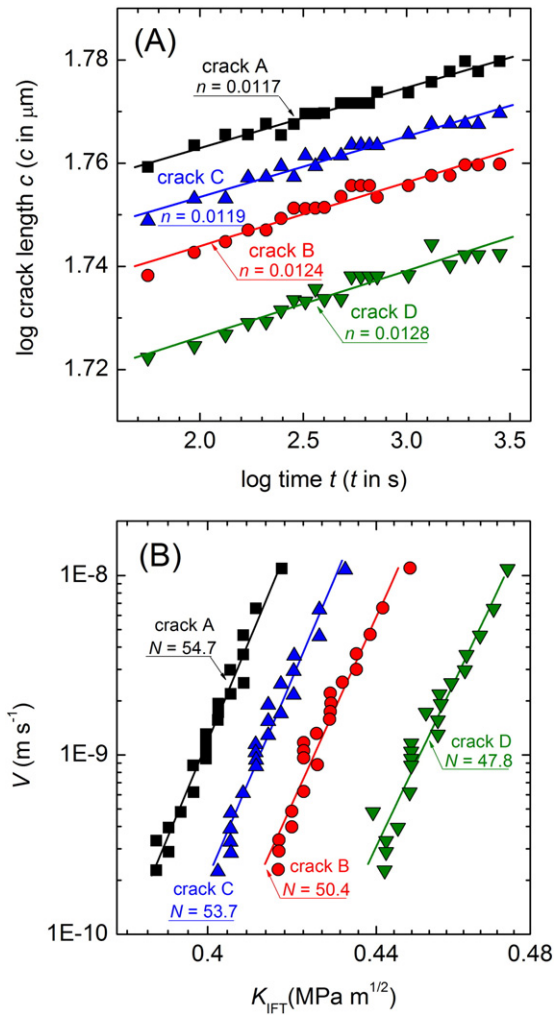

Fig. 9. Double logarithmic presentation of the crack length c vs. time t (A) and crack growth rate V vs. the calculated stress intensity factor K_{IFT} (B) of the four cracks of Fig. 8.

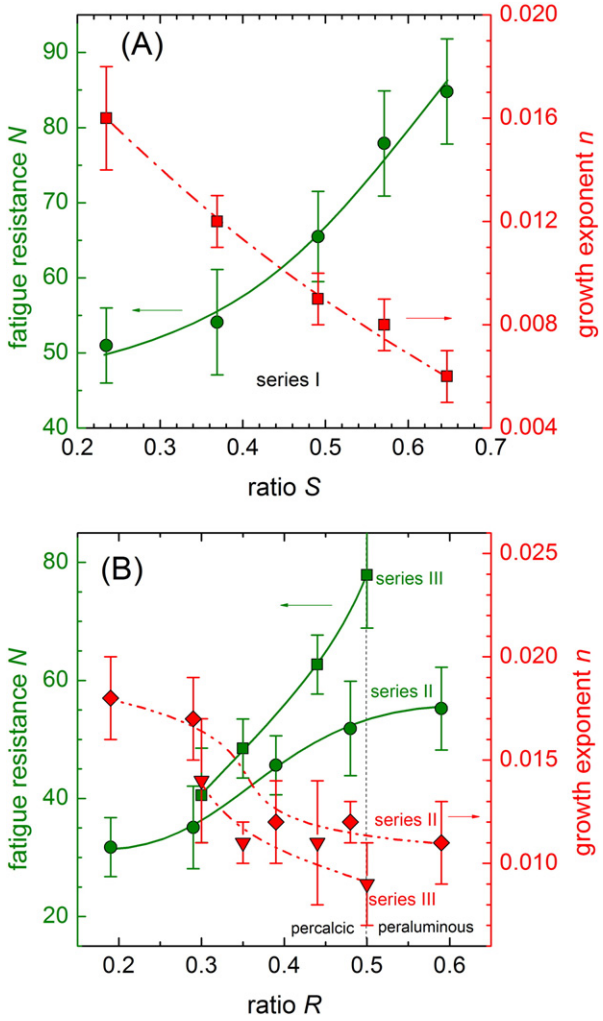

Fig. 10. Dependence of the fatigue resistance N and the growth exponent n on the compositional ratios S (A) and R (B). Lines are intended as visual guides.

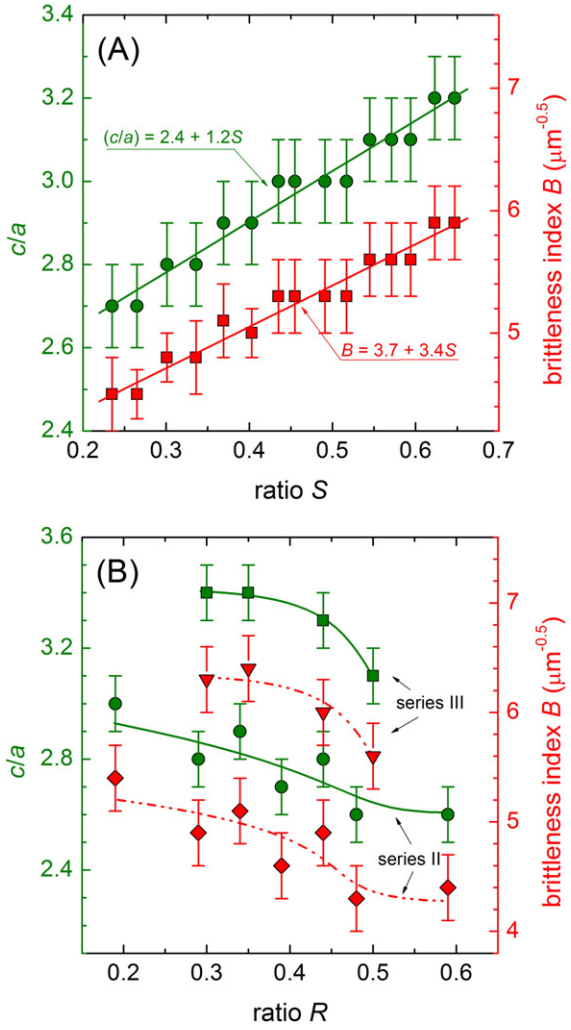

Fig. 11. Crack length-to-indent size ratio c/a and brittleness index B for compositional ratios S (A) and R (B). Lines are intended as visual guides.

increases with the substitution of aluminium for silicon in the network. For compositions along the meta-aluminous join (series I) the dependence of H_V on S follows the linear equation H_V (GPa) = 5.79 + 2.1S (Fig. 5A). H_V shows a steep increase at $R \approx 0.5$ when passing the meta-aluminous join from the percalcic to the peraluminous side of the CAS system (series II and III, Fig. 5B). H_V data of series I–III glasses are listed in Table 3.

4.4. Crack initiation

Fig. 6A (right side) shows exemplarily the cracking patterns around three Vickers imprints of glass $R = 0.44$ (series III) after indentation at loads of 0.2, 0.7 and 1.2 N, respectively. An increase in the number of radial-median cracks with increasing load can be observed (subsurface lateral cracks may not be visible). The left side of Fig. 6A shows that the crack probability F decreases while the critical load to generate radial-median cracks P_0 increases with increasing ratio R (series II and III). An increase in crack resistance for CAS glasses with increasing Al-to-Ca ratio but constant SiO_2 content is also evident in series II where F seems to decrease strongly on the peraluminous side (Fig. 6B). The change in the compositional trend at $R = 0.5$ seems to be in line with the changes observed in the elastic constants and in hardness of these glasses. For glasses on the meta-aluminous join (series I) F shows a noticeable minimum at around $S = 0.5$ (Fig. 7A). Thus, glasses of the anorthite composition ($CaO:Al_2O_3:SiO_2 = 1:1:2$) exhibit a crack resistance $CR > 5$ N. It should be noted that for series I and II, P_0 is generally larger than 1.5 N and cracking evolves from $F = 0$ to $F = 100\%$ only in three load stages of the employed indenter, which impedes Weibull statistics of a sigmoidal-like course of $F(P)$ as shown in Fig. 6A. Therefore Figs. 6B, 7A and B show the crack probability for each load only. To test the influence of humidity on the crack initiation, glasses of series I were also indented under nitrogen gas (RH = 10^{-4}–10^{-6}%). Fig. 7B shows that radial-median cracking is less probable under the dry environment but the compositional trend of highly resistant glasses for $S \approx 0.5$ is preserved.

4.5. Sub-critical crack growth

Fig. 8 shows the increase in crack length c with time of four radial cracks initiated at the corners of a Vickers indent ($P = 4.9$ N) of glass $R = 0.35$ (series III). Within the observation period of 56–2820 s, cracks A–D (denoting the cracks from each of the four corners) propagate nearly the same distance of 2–3 μm, whereas they notably differ in the length of the immediately formed cracks (0–56 s). This is taken as a consequence of different initiation times, influences of neighbouring cracking events and early branching within the plastic deformation zone (visible, e.g., on the cracks at the corners A and B, Fig. 8). Fig. 9 shows

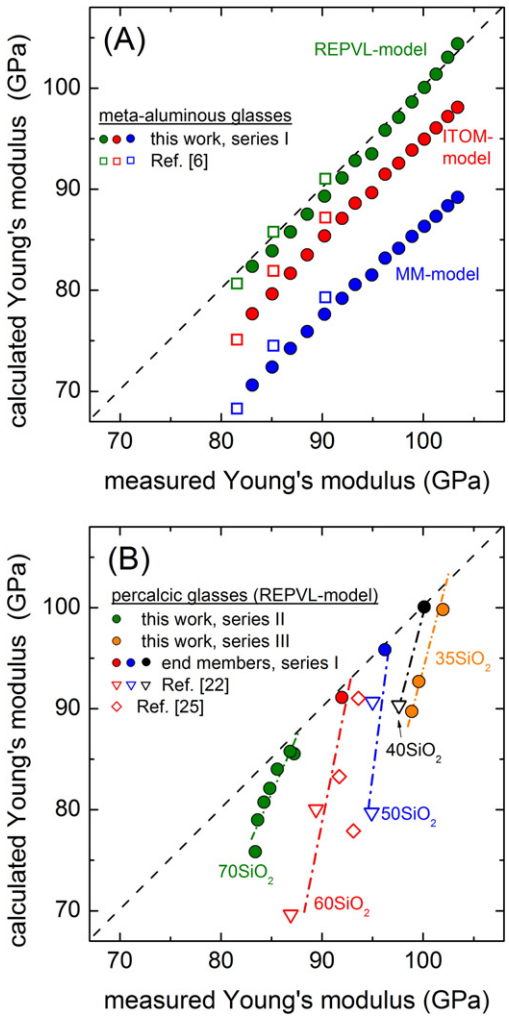

Fig. 12. Measured vs. calculated Young's modulus E for CAS glasses of meta-aluminous (A) and percalcic (B) composition. Calculation of E was performed using MM model Eqs. (16)–(17) with $m = 1$, the REPVL model Eqs. (16), (18) with $m = 1$ and ITOM model Eq. (16) with $m = 1.1$. Ionic radii: 135 pm (O^{II}), 100 pm (Ca^{VI}), 39 pm (Al^{IV}) and 26 pm (Si^{IV}) [46]. For percalcic glasses only results of REPVL model calculation are shown. Iso-compositional lines (molar fraction of SiO_2 in %) are intended as visual guides. Dashed black line indicate unity between calculated and measured E data.

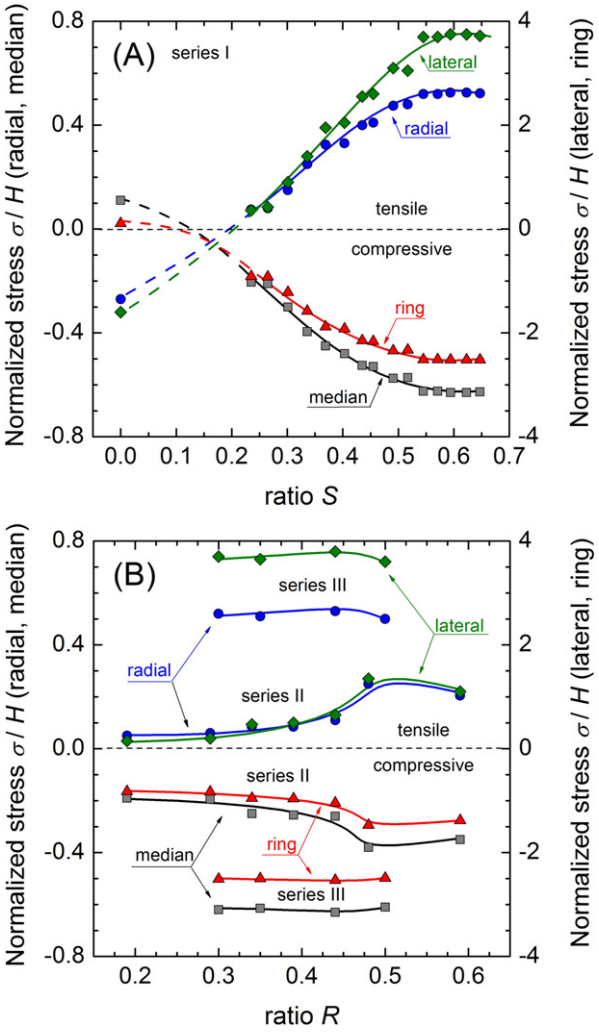

Fig. 13. Stress components (loading) at the rim of the imprint ($r = a$) governing radial and median (left ordinate) as well as ring and subsurface lateral cracks (right ordinate) as a function of the compositional ratios S (A) and R (B). Tensile (+) and compressive (−) stress components are extracted from contour plots of Fig. 4 of Ref. [53] using E-to-H and Poisson's ratios of Tables 2 and 3 for series I–III. Input data for silica glass (Heraeus HOQ 310) are taken from reference measurements with $E = 73.1$ GPa, $H_V = 6.5$ GPa and $\mu = 0.166$.

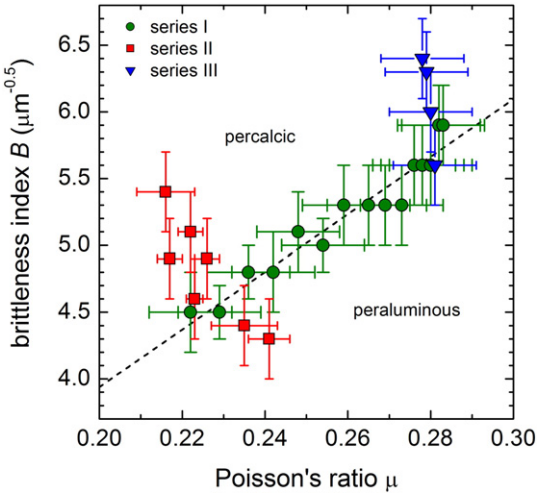

Fig. 14. Brittleness index B versus Poisson's ratio μ. The dashed line is the linear dependence $B = 21.6\mu - 0.37$ fitted through the data of series I (meta-aluminous glasses) of regression coefficient $R^2 = 0.94$.

the $c(t)$- and $V(K_{IFT})$-dependencies for cracks A–D. The parallel lines in Fig. 9A and B indicate only small differences (up to 9%) in the growth and fatigue parameters n and N (Table 3).

Averaged growth data from up to 8 cracks (two imprints) for each glass were used in Fig. 10 to visualize the compositional dependence of the fatigue and growth parameters N and n. For series I it is found that the fatigue resistance N increases progressively with increasing S from 51 to 84 (Fig. 10A). Vice versa, the growth exponent decreases within the same compositional range from 0.016 to 0.006 (Table 3), indicating less pronounced sub-critical growth for glasses with increasing substitution of aluminium for silicon in the network. For series II and III it can be seen from Fig. 10B that percalcic glasses exhibit a lower fatigue resistance and a higher growth exponent than peraluminous glasses of the same silica content.

4.6. Brittleness

Fig. 11 shows the brittleness index B and the c-to-a ratio of the CAS glasses. On the meta-aluminous join (series I) both parameters increase linearly with increasing S (Fig. 11A). The data are best fitted by the equations $(c/a) = 2.4 + 2.1S$ and $B = 3.7 + 3.4S$ (B in $\mu m^{-0.5}$), respectively. For glasses of constant SiO_2 content, both parameters show a non-linear dependence with decreasing values from the percalcic to peraluminous side (Fig. 11B). c/a and B data of series I–III are compiled in Table 3.

5. Discussion

The results reveal characteristic changes in the elastic properties of glasses in the intermediate-silica range of the CAS system. In series I the compositional dependency of the elastic properties, expressed through the ratio S, has been found to be mostly linear. In series II and III, non-linear or step-like dependencies where observed, using the compositional parameter of R. These observations are related to the chemical dependence of glass structure.

It is widely thought that elastic constants are governed by the pertinent short-range structure, as they are governed by inter-atomic forces and the packing density of their oxide constituents [19,21,22]. For Young's modulus, Fig. 12A shows that the empirical models of Makishima–Mackenzie (MM) [19], Rocherulle–Ecolivet–Poulain–Verdier–Laurent (REPVL) [21] and Inaba–Todaka–Otha–Morinaga (ITOM) [22] fit the dependence of series I relatively well. However, series II and III do not follow these simplistic predictions (Fig. 12B). The failure of the models for percalcic compositions becomes even more pronounced if CAS glasses from literature [6,22,25] (for composition see Fig. 1) are included in the analysis. Due to the low number of data points on the peraluminous side a corresponding analysis is not shown. The result for percalcic glasses in which calcium is present in excess of aluminium and non-bridging oxygen (NBO) are formed shows that further parameters in the models are necessary to predict the elastic behaviour correctly. From a structural viewpoint one can think of mid-range related parameters reflecting the network topology such as Q-group distribution and framework cation ordering. For the series with constant SiO_2 content, changes in the Q-group distribution are expected due to the preference of aluminium for Q^4 groups. Thus, with increasing R ratio, disproportionation of Q^3 groups into Q^4 and Q^2 groups is more likely. In contrast, on the meta-aluminous join only Q^4 groups are present (nominally NBO-free). Other effects may arise from ordering of framework cations. The ordering of framework Si and Al cations in aluminosilicates is often described in terms of the Löwenstein avoidance principle, which rejects the existence of Al–O–Al linkages. For meta-aluminous glasses Navrotsky et al. [48] found that with increasing field strength of the charge balancing cation the enthalpy of ordering decreases, shifting the Eq. (2)(Si–O–Al) ↔ Al–O–Al + Si–O–Si to the right side. The volume effect of mixing aluminium and silicon framework units can be seen by the negative deviation from linear additivity

of the molar volume of series I in Fig. 2A. Using NMR, Lee and Stebbins [49] confirmed the thermochemical considerations by detecting more Al–O–Al and Si–O–Si sites in CAS glasses than in alkali aluminosilicates. The increase in network disordering depends on composition as the degree of Al avoidance increases with the *S* ratio [49]. For percalcic and meta-aluminous glasses, Neuville et al. [11] finds up to 8% 5-fold coordinated Al (on the peraluminous side its portion increases rapidly), which adds further constraints to framework cation ordering.

We note that the calculated values of *E* depend strongly on the selected ionic radii. We have employed the effective ionic radii of Shannon published in 1976 [46] for the coordination numbers 6, 4, 4 and 2 for Ca, Al, Si and O respectively. Using the classical crystal radii of Pauling [50], which are somewhat larger, the *E* curves of Fig. 12A and B shift by ~9 GPa to higher values, but their compositional trends remain unchanged (not shown). Further, we have taken into account small fractions of 5-fold coordinated aluminium (5–8%) in the calculus, which are reported in NMR studies for percalcic and charge balanced CAS glasses [11]. This correction led only to small changes in the calculated values of the Young's modulus (within the symbol size of Fig. 12A and B). AlO_5 was introduced in the calculation by taking the mean value (359.5 kcal mol^{-1}, i.e. per unit volume 27.8 kcal/cm^{-3}) of Sun's dissociation energy range (402–317 kcal mol^{-1}) [51] which is listed for tetrahedrally and octahedrally coordinated aluminium and the ionic radius of 48 pm for aluminium cations with the coordination number of five [46].

Fig. 7 shows that the probability to radial-median cracking decreases with increasing *S* and *R* ratios in series I, II and III respectively (in series I only up to $S = 0.5$). Further Fig. 6 shows that glasses of series II are more resistant to cracking than those of series III. To understand these differences one may calculate the driving force for indentation cracking. Rouxel and co-workers [52–54] showed that the driving force for indentation cracking can be traced (outside of the densified zone) to normal tensile stresses (opening-mode of fracture), which occur upon peak load. Depending on the mechanical properties of the glass, i.e., *E*/*H* and μ parameters, the stress components normal to the direction of radial, median, ring and subsurface lateral cracks outside the deformation zone are either zero, tensile or compressive. Zero stresses in all directions provide explanation scheme for resilient (damage-resistant) glasses. Changes in crack patterns with composition occur when corresponding stress components change their sign. We note that micro-cracking can occur also upon unloading, if the sign of a particular stress component changes from negative to positive during that stage [55]. Fig. 13 shows the situation for the loading stage only. Stress components are normalized to hardness and were derived from the contour plots of Ref. [53] using *E*-to-H_V and Poisson's ratios of Tables 2 and 3 for series I–III. Inspection of Fig. 13 predicts radial and lateral cracking of the tested CAS glasses as their stress components are positive (tensile stresses). This is in agreement with the observed cracking patterns in which radial-median cracks at the corner of the imprints dominate on the post-indentation surface (see Figs. 6 and 8). With increasing *S* the tensile stresses governing radial and sub-surface lateral cracks increase up to an apparent maximum at around $S = 0.6$ (Fig. 13A). Further, it can be seen from Fig. 13B that the relevant tensile stresses are larger for series II than for series III glasses. Expanding the compositional range on the meta-aluminous join (series I) to $S = 0$ (silica glass) a change in the cracking pattern from radial-lateral (this work) to median-cone cracking is found for glasses of composition $S = 0.1$–0.2 (Fig. 13B). For the transition range the driving forces are predicted to vanish. Here, glasses are expected to exhibit a high crack initiation load and a less brittle character. Gross et al. [6] have investigated the crack resistance in the high-silica range of the CAS system ($0 \le S \le 0.2$). For $S = 0.2$ (10CaO, $10Al_2O_3$, $80SiO_2$ in mol%) they found a maximum of the crack initiation load, which confirms the proposed crossover in charge balanced CAS glasses. Although these correlations underline the governing influence of tensile stresses for the occurrence of micro-cracks, the decrease of the crack probability with *S* for silica-rich glasses of series I cannot be explained from the above stress analysis alone. Also, it is found that percalcic glasses are less resistant to radial-median cracking than peraluminous glasses. Thus, other factors contribute to crack generation in CAS glasses. Among these, we count environmental effects, such as most strictly shown in Fig. 7. Fig. 7 shows a dramatic decrease in *F* if water is excluded from the testing atmosphere. The effect of the water partial pressure on fatigue has been previously reported for commercial alkaline earth aluminosilicate glass with varying fictive temperature [38]. Also Gross et al. [6] postulated that the water sensitivity, besides low elastic moduli dependence on fictive temperature, contributes to low crack resistance.

Besides crack initiation, also crack growth was found to depend on the composition of the CAS glasses. Fig. 10 shows an increase of the fatigue resistance *N* (decrease in the growth exponent *n*) with either increasing *S* or *R* for all three series. The compositional course of the fatigue parameters follow the expected trend that glasses with decreasing portion of NBO are less prone to water attack (series II and III) and that frameworks of mixed Si-/Al-units are energetically more favourable [48] and also closer packed (due to stuffing with Ca ions), which may slow down diffusion of water molecules [56] and thereby hamper hydration of the glass at the crack-tip (series I).

Based on the definition brittleness parameters such as *B* and the *c*-to-*a* ratio are closer related to the deformation process itself, i.e. the densification vs. shear contribution under and beneath the imprint. It was shown in recent studies that μ is obviously playing a key role in the indentation behaviour of glasses [57–59] as it is also the determining materials characteristic in the analysis of the driving forces for indentation cracking [52–54]. For glasses of series I, μ increases with increasing *S* ratio, and μ of series III is generally larger than for series II. Thus, with increasing *S* (series I) one would expect that the contribution of volume conservative flow increases and the degree of material densification decreases. The lower compressibility of glasses with higher *S* ratio can be related to the increase in the *APF* since the glass structure is becoming stuffed by calcium ions when aluminium is substituting silicon in the framework. Vice versa, the more open structure of silica-rich CAS glasses on that join allows for larger compaction under the indenter. Higher contributions of shear flow to the total deformation are also expected in series III as compared to series II (0.35 versus 0.7 mol% SiO_2). With more pronounced shear flow one would also expect a greater ease for cracking and, thus, a more brittle character of the glasses. Fig. 11 shows that the compositional course of *B* and *c*/*a* of series I is in agreement with this. On the other hand, one would expect that percalcic glasses with lower Poisson's ratio are less brittle. In contrast, these glasses exhibit in the indentation experiment a more pronounced brittleness than the meta-aluminous and peraluminous glasses of similar μ. The deviation from the expected trend of the percalcic and peraluminous glasses can be seen from Fig. 14 where the brittleness index *B* is plotted as a function of the Poisson's ratio of all three series of CAS glasses. As in case of the elastic constants we assume that on the percalcic side the increasing fraction of NBO together with changes in the silicon speciation contribute to the higher brittleness while on the peraluminous side the higher fraction of 5-fold coordinated aluminium leads to a higher connectivity and lower brittleness of the glasses.

6. Conclusions

Experimental values of the elastic constants of CAS glasses were compared with those calculated in terms of existing theories. Empirical models relate bulk elastic moduli of glasses to the inter-atomic forces and the packing density of their oxide constituents. Interrelations between elastic constants (hardness) and the chemical dependence of structure were found to be in agreement with these models for meta-aluminous glasses, while deviations between the observed and predicted values are evident for percalcic compositions. The result shows that the network topology, which is not yet implemented in the tested

models, plays an important role in the understanding of bulk mechanical behaviour of glasses and shall be further parameterized.

Stresses at the rim of the indent as derived from bulk mechanical data and hardness values were compared with the probability to initiate cracks. The analysis showed that crack patterns of CAS glasses after Vickers indentation follow in principle the predicted trend (radial-median cracking) for so-called normal glasses but the ease for cracking seems to be strongly dependent on the environmental conditions as reference measurements under dry nitrogen gas showed.

An unexpected trend of percalcic and peraluminous glasses of constant SiO_2 fraction is evident as their brittleness index seems to decrease with increasing Poisson's ratio although they are prone to radial-median cracking (crack patterns of normal glasses). Changes in connectivity in mixed network former glasses caused by excess and deficient fractions of network modifiers may contribute to this behaviour.

Finally, one may use the results to propose simple compositional guidelines on how to improve mechanical properties of CAS glasses in the intermediate-silica range: Meta-aluminous and peraluminous glasses are found to offer superior mechanical properties as they combine high stiffness with low fatigue. Al-deficient glasses (percalcic side of the CAS system) appear to be less beneficial with respect to these properties as their structure is less connected (Q-group distribution) and prone to water–crack interaction at the surface. Among the meta-aluminous compositions a minimum in fatigue is evident for glasses close to the anorthite stoichiometry ($S = 0.5$), while elastic moduli and hardness increase with increasing S on that join even for glasses Al-richer than the feldspar composition ($S > 0.5$).

Acknowledgements

The financial support of the Deutsche Forschungsgemeinschaft (DFG) by the Priority Programme 1594 is gratefully acknowledged.

References

[1] J.A. Sampaio, M.L. Baesso, S. Gama, A.A. Coelho, J.A. Eiras, I.A. Santos, Rare earth doping effect on the elastic moduli of low silica calcium aluminosilicate glasses, J. Non-Cryst. Solids 304 (2002) 293–298.
[2] L.G. Hwa, K.J. Hsieh, L.C. Liu, Elastic moduli of low-silica calcium alumino-silicate glasses, Mater. Chem. Phys. 78 (2002) 105–110.
[3] F.T. Wallenberger, S.D. Brown, High-modulus glass fibers for new transportation and infrastructure composites and new infrared uses, Compos. Sci. Technol. 51 (1994) 243–263.
[4] J.A. Topping, Glass-ceramics from the system $CaO–Al_2O_3–SiO_2$, Am. Ceram. Soc. Bull. 56 (1977) 574-574.
[5] G.H. Beall, Design and properties of glass-ceramics, Annu. Rev. Mater. Sci. 22 (1992) 91–119.
[6] T.M. Gross, M. Tomozawa, A. Koike, A glass with high crack initiation load: role of fictive temperature-independent mechanical properties, J. Non-Cryst. Solids 355 (2009) 563–568.
[7] C.I. Merzbacher, W.B. White, The structure of alkaline earth aluminosilicate glasses as determined by vibrational spectroscopy, J. Non-Cryst. Solids 130 (1991) 18–34.
[8] C.I. Merzbacher, K.J. McGrath, P.L. Higby, ^{29}Si NMR and infrared reflectance spectroscopy of low-silica calcium aluminosilicate glasses, J. Non-Cryst. Solids 136 (1991) 249–259.
[9] S. Takahashi, D.R. Neuville, H. Takebe, Thermal properties, density and structure of percalcic and peraluminus $CaO–Al_2O_3–SiO_2$ glasses, J. Non-Cryst. Solids 411 (2015) 5–12.
[10] D.R. Neuville, L. Cormier, D. Massiot, Al environment in tectosilicate and peraluminous glasses: a ^{27}Al MQ-MAS NMR, Raman, and XANES investigation, Geochim. Cosmochim. Acta 68 (2004) 5071–5079.
[11] D.R. Neuville, L. Cormier, D. Massiot, Al coordination and speciation in calcium aluminosilicate glasses: effects of composition determined by ^{27}Al MQ-MAS NMR and Raman spectroscopy, Chem. Geol. 229 (2006) 173–185.
[12] L. Cormier, D.R. Neuville, G. Calas, Structure and properties of low-silica calcium aluminosilicate glasses, J. Non-Cryst. Solids 274 (2000) 110–114.
[13] N. Jakse, M. Bouhadja, J. Kozaily, J.W.E. Drewitt, L. Hennet, D.R. Neuville, H.E. Fischer, V. Cristiglio, A. Pasturel, Interplay between non-bridging oxygen, triclusters, and fivefold Al coordination in low silica content calcium aluminosilicate melts, Appl. Phys. Lett. 101 (2012) 201903.
[14] D.R. Neuville, L. Cormier, A.M. Flank, V. Briois, D. Massiot, Al speciation and Ca environment in calcium aluminosilicate glasses and crystals by Al and Ca K-edge X-Ray absorption spectroscopy, Chem. Geol. 213 (2004) 153–163.
[15] G.S. Henderson, D.R. Neuville, L. Cormier, An O K-edge XANES study of glasses and crystals in the $CaO–Al_2O_3–SiO_2$ (CAS) system, Chem. Geol. 259 (2009) 54–62.
[16] G. Engelhardt, M. Nofz, K. Forkel, F.G. Wihsmann, M. Mägi, A. Samoson, E. Lippmaa, Structural studies of calcium aluminosilicate glasses by high resolution solid state ^{29}Si and ^{27}Al magic angle spinning nuclear magnetic resonance, Phys. Chem. Glasses 26 (1985) 157–165.
[17] D.R. Neuville, L. Cormier, V. Montouillout, D. Massiot, Local Al site distribution in aluminosilicate glasses by ^{27}Al MQMAS NMR, J. Non-Cryst. Solids 353 (2007) 180–184.
[18] J.F. Stebbins, X. Xue, NMR evidence for excess non-bridging oxygen in an aluminosilicate glass, Nature 390 (1997) 60–62.
[19] A. Makishima, J.D. Mackenzie, Direct calculation of Young's modulus of glass, J. Non-Cryst. Solids 12 (1973) 35–45.
[20] A. Makishima, J.D. Mackenzie, Calculation of bulk modulus, shear modulus and Poisson's ratio of glass, J. Non-Cryst. Solids 17 (1975) 147–157.
[21] J. Rocherulle, C. Ecolivet, M. Poulain, P. Verdier, Y. Laurent, Elastic moduli of oxynitride glasses – extension of Makishima and Mackenzie's theory, J. Non-Cryst. Solids 108 (1989) 187–193.
[22] S. Inaba, S. Todaka, Y. Otha, K. Morinaga, Equation for estimating the Young's modulus, shear modulus and Vickers hardness of aluminosilicate glasses, J. Jpn. Inst. Metals 64 (2000) 177–183.
[23] L.G. Hwa, Rayleigh–Brillouin scattering in calcium aluminosilicate glasses, J. Raman Spectrosc. 29 (1998) 269–272.
[24] L.G. Hwa, C.L. Lu, L.C. Liu, Elastic moduli of calcium alumino-silicate glasses studied by Brillouin scattering, Mater. Res. Bull. 35 (2000) 1285–1292.
[25] R.J. Eagan, J.C. Swearekgen, Effect of composition on the mechanical properties of aluminosilicate and borosilicate glasses, J. Am. Ceram. Soc. 61 (1978) 27–30.
[26] L. Wondraczek, J.C. Mauro, J. Eckert, U. Kühn, J. Horbach, J. Deubener, T. Rouxel, Towards ultra-strong glasses, Adv. Mater. 23 (2011) 4578–4586.
[27] H.J. McSkimin, Pulse superposition method for measuring ultrasonic wave velocities in solids, J. Acoust. Soc. Am. 33 (1961) 12–16.
[28] J. Deubener, H. Bornhöft, S. Reinsch, R. Müller, J. Lumeau, L.N. Glebova, L.B. Glebov, Viscosity, relaxation and elastic properties of photo-thermo-refractive glass, J. Non-Cryst. Solids 355 (2009) 126–131.
[29] G.V. Blessing, Dynamic elastic modulus measurements in materials, ASTM STP 1045, ASTM, Philadelphia, PA, USA, 1990.
[30] S. Striepe, N. Da, J. Deubener, L. Wondraczek, Micromechanical properties of (Na,Zn)-sulfophosphate glasses, J. Non-Cryst. Solids 358 (2012) 1032–1037.
[31] S. Striepe, M.M. Smedskjaer, J. Deubener, U. Bauer, H. Behrens, M. Potuzak, R.E. Youngman, J.C. Mauro, Y. Yue, Elastic and micromechanical properties of isostatically compressed soda–lime–borate glasses, J. Non-Cryst. Solids 364 (2013) 44–52.
[32] R. Limbach, B.P. Rodrigues, L. Wondraczek, Strain-rate sensitivity of glasses, J. Non-Cryst. Solids 404 (2014) 124–134.
[33] B.R. Lawn, D.B. Marshall, Hardness, toughness, and brittleness — an indentation analysis, J. Am. Ceram. Soc. 62 (1979) 347–350.
[34] J. Sehgal, Y. Nakao, H. Takahashi, S. Ito, Brittleness of glasses by indentation, J. Mater. Sci. Lett. 14 (1995) 167–169.
[35] M. Wada, H. Furukawa, K. Fujita, Crack resistance of glass on Vickers indentation, Proc. X Int. Congr. Glass 1974, pp. 39–46.
[36] S. Yoshida, A. Hidaka, J. Matsuoka, Crack initiation behavior of sodium aluminosilicate glasses, J. Non-Cryst. Solids 344 (2004) 37–43.
[37] S. Yoshida, T. Hayashi, T. Fukuhara, K. Soeda, J. Matsuoka, N. Soga, Scratch test for evaluation of surface damage in glass, in: R.C. Bradt, D. Munz, M. Sakai, K.W. White (Eds.), Fracture Mechanics of Ceramics, vol. 14, Springer 2005, pp. 101–111.
[38] S. Striepe, J. Deubener, M.M. Smedskjaer, M. Potuzak, Environmental effects on fatigue of alkaline earth aluminosilicate glass with varying fictive temperature, J. Non-Cryst. Solids 379 (2013) 161–168.
[39] S. Dériano, A. Jarry, T. Rouxel, J.C. Sangleboeuf, S. Hamshire, The indentation fracture toughness (K_C) and its parameters: the case of silica-rich glasses, J. Non-Cryst. Solids 344 (2004) 44–50.
[40] S. Striepe, J. Deubener, Effect of lithium-to-magnesium ratio in metaphosphate glasses on crack-tip condensation and sub-critical crack growth, J. Non-Cryst. Solids 375 (2013) 47–54.
[41] K. Niihara, R. Morena, D.P.H. Hasselman, Evaluation of K_{Ic} of brittle solids by the indentation method with low crack-to-indent ratios, J. Mater. Sci. Lett. 1 (1982) 13–16.
[42] G.D. Quinn, R.C. Bradt, On the Vickers indentation fracture toughness test, J. Am. Ceram. Soc. 90 (2007) 673–680.
[43] R.O. Ritchie, The conflicts between strength and toughness, Nat. Mater. 10 (2011) 817–822.
[44] P. Vullo, M.J. Davis, Comparative study of micro-indentation and Chevron notch fracture toughness measurements of silicate and phosphate glasses, J. Non-Cryst. Solids 349 (2004) 180–184.
[45] S.M. Wiederhorn, Mechanisms of subcritical crack growth in glass, in: R.C. Bradt, D.P.H. Hasselman, F.F. Lange (Eds.), Fracture Mechanics of Ceramics, vol. 4, Plenum Press, New York 1978, pp. 549–580.
[46] R.D. Shannon, Revised effective ionic radii and systematic studies of interatomic distances in halides and chalcogenides, Acta Crystallogr. Sect. A 32 (1976) 751–767.
[47] F.A. Seifert, B.O. Mysen, D. Virgo, Three-dimensional network structure of quenched melts (glass) in the systems $SiO_2–NaAlO_2$, $SiO_2–CaAl_2O_4$ and $SiO_2–MgAl_2O_4$, Am. Mineral. 67 (1982) 696–717.
[48] A. Navrotsky, G. Peraudeau, P. McMillan, J.P. Coutures, A thermochemical study of glasses and crystals along the joins silica–calcium aluminate and silica–sodium aluminate, Geochim. Cosmochim. Acta 46 (1982) 2039–2047.
[49] S.K. Lee, J.F. Stebbins, Al–O–Al and Si–O–Si sites in framework aluminosilicate glasses with Si/Al = 1: quantification of framework disorder, J. Non-Cryst. Solids 270 (2000) 260–264.
[50] L. Pauling, Nature of Chemical Bond and Structure of Molecules and Crystals, second ed. Cornell University Press, Ithaca, N.Y., 1940

[51] K.H. Sun, Fundamental condition of glass formation, J. Am. Ceram. Soc. 30 (1947) 277–281.
[52] P. Sellappan, T. Rouxel, F. Celarie, E. Becker, P. Houizot, R. Conradt, Composition dependence of indentation deformation and indentation cracking in glass, Acta Mater. 61 (2013) 5949–5965.
[53] T. Rouxel, P. Sellappan, F. Celarie, P. Houizot, J.C. Sangleboeuf, Toward glasses with better indentation cracking resistance, C. R. Mec. 342 (2014) 46–51.
[54] T. Rouxel, Driving force for indentation cracking in glass: composition, pressure and temperature dependence, Phil. Trans. R. Soc. A 373 (2015) 20140140.
[55] S. Yoshida, M. Kato, A. Yokota, S. Sasaki, A. Yamada, J. Matsuoka, N. Soga, C.R. Kurkjian, Direct observation of indentation deformation and cracking of silicate glasses, J. Mater. Res. 30 (2015) 2291–2299.
[56] S. Reinsch, R. Müller, J. Deubener, H. Behrens, Internal friction of hydrated soda–lime–silicate glasses, J. Chem. Phys. 139 (2013) 174506.
[57] S. Yoshida, J.C. Sangleboeuf, T. Rouxel, Quantitative evaluation of indentation-induced densification in glass, J. Mater. Res. 20 (2005) 3404–3412.
[58] T. Rouxel, H. Ji, J.P. Guin, F. Augereau, B. Ruffle, Indentation deformation mechanism in glass: densification versus shear flow, J. Appl. Phys. 107 (2010) 094903.
[59] G.N. Greaves, A.L. Greer, R.S. Lakes, T. Rouxel, Poisson's ratio and modern materials, Nat. Mater. 10 (2011) 823–837.